Electronic Supplementary Information

Crystal phase and band edge modulation of MA- and Br-free CsFA-based perovskite for efficient inverted solar cells and minimodules

Jiewei Yang[a], Qi Wang[a], Wei Hui[b], Xin Chen[a], Yuqi Yao[a], Weijian Tang[c], Wuke Qiu[a], Xiaopeng Xu[a], Lin Song[b], Yihui Wu*[a], and Qiang Peng*[a]

[a] School of Chemical Engineering, State Key Laboratory of Polymer Materials Engineering, Engineering Research Center of Alternative Energy Materials & Devices, Ministry of Education, Sichuan University, Chengdu 610065, P. R. China

[b] Frontiers Science Center for Flexible Electronics (FSCFE), Institute of Flexible Electronics (IFE), Northwestern Polytechnical University, Xi'an 710072, P. R. China

[c] College of Materials Science and Engineering, Sichuan University, Chengdu 610065, P. R. China

*E-mails: yihuiwu@scu.edu.cn (Y.W.); qiangpeng@scu.edu.cn (Q.P.)

1. Materials

All the chemicals were used as received in this study. Lead iodide (≥99.999%), formamidinium iodide (FAI, 99.9%), NiO_x nanoparticle (99.999%), and C60 (99.5%) were purchased from Advanced Election Technology Co. Ltd. Ethanol (≥99.5%, anhydrous), anisole (99.7%, anhydrous), and (Methyl methylsulfinyl) methyl sulfide (MMS, >96.0%) were purchased from Aladdin. 2-Propanol (IPA, 99.5%), Chlorobenzene (CB, 99.8%, anhydrous), Dimethylformamide (DMF, 99.8%, anhydrous), and Dimethy sulfoxide (DMSO, ≥99.9%, anhydrous) were purchased from Sigma-Aldrich. Cesium iodide (CsI, 99.999%) was purchased from Alfa-Aesar. Lead (II) chloride ($PbCl_2$, 99.9%), phenethylammonium iodide (PEAI, 99.5%), and Bathocuproine (BCP, 99%) were purchased from Xi'an Yuri Solar Co. Ltd. 1,3-Diaminopropane Dihydroiodide ($PDAI_2$, ≥99.5%) was purchased from Xi'an e-Light New Material Co, Ltd. (4-(3,6-dimethyl-9H-carbazole-9-yl)butyl) phosphonic acid (Me-4PACz, >99.0%) was purchased from TCI. Hydrogen peroxide (H_2O_2, ≥30%) was purchased from RESO. All the solvents are used directly without further purification.

2. Device fabrication

Perovskite solar cells were fabricated on the cleaned and patterned FTO substrates (AGC22-8A, Advanced Election Technology Co. Ltd.). To prepare NiO_x hole-transport layer: 10 mg/mL of NiO_x aqueous solution (40 mol.% H_2O_2 was added) was ultrasonic treated at low temperature (about 5 ^oC) for 30 min and filtered with 0.22 μm PTFE filter to gain NiO_x dispersion solution. Before depositing NiO_x, FTO substrates were treated by UV-Ozone for 20 min. Then, the NiO_x solution was spin-coated on the FTO substrates at 2000 rpm for 40 s and annealed at 120 ^oC for 15 min. After that, 0.5 mg/mL of Me-4PACz/ethanol solution was deposited on the NiO_x film at 3000 rpm for 30 s and annealed at 110 °C for 10 min to form the bilayer hole-transport layers.

The perovskite solution was prepared by mixing 782.0 mg of PbI_2, 277.6 mg of FAI, 22.0 mg of CsI and 24.0 mg of $PbCl_2$ in 1 mL of a mixed solvent (DMF: DMSO = 4:1, v/v), which was stirred for 2 h before use. For the target perovskite solution, 10 μL of MMS was added directly to the precursor by replacing the same amount of DMSO. The perovskite solution was filtered with 0.22 μm PTFE filter. Before depositing the perovskite solution, 1 mg/mL of PEAI/DMF solution was deposited on the above-mentioned substrates by spin-coating at 4000 rpm for 20 s to improve the wettability of the substrate. After that, the perovskite ink was deposited on the substrate by spin-coating at 1000 rpm for 8 s with a ramp of 200, and 5000 rpm for 25 s (2000 rpm ramp). 20 s into the second step, 120 μL of anisole was

deposited onto the substrate. The wet film was annealed at 110 °C for 20 min. After the perovskite film was cooled down to room temperature, 1 mg/mL of $PDAI_2$/(IPA:CB = 1:1, v/v) solution was deposited via spin-coating at 4500 rpm for 25 s and annealed at 110 °C for 5 min. Finally, 20 nm of C60, 6 nm of BCP, and 120 nm of Ag electrode were sequentially deposited by thermal evaporation. After that, a layer of MgF_2 (around 140 nm) was thermal deposited on the glass side as the anti-reflection coating.

For the minimodule, a vacuum-assisted method was adopted to fabricate the large-area perovskite film. Briefly, the perovskite precursor was uniformly spreaded on the substrate with HTL and then spin-coated with a two-step process. The first step was 1000 rpm for 8 s with an acceleration of 200 rpm/s. The second step was 5000 rpm for 10 s with a ramp-up of 2000 rpm/s. The as-obtained wet perovskite film was put into a sample chamber which is connected to a pump system. Once the valve is turned on, the solvent was removed rapidly under a low pressure maintained at 10 Pa for 10 s. After turning off the valve, the brown and transparent perovskite film is placed onto the hot plate. The perovskite films were annealed at 110 ºC for 20 min. All other processing technologies were kept the same as those of the small size perovskite device. A perovskite module with 6 series sub-cells was fabricated on an FTO glass substrate with a size of 5×5 cm^2. The series interconnection of modules was realized through P1, P2, and P3 lines. Pattern the lines using a laser scribing system with a wavelength of 1064 nm, a frequency of 20 KHz, and a scan speed of 2000. For P1 line, a power of 16 W was used and the FTO substrate was scribed 30 times. For P2 line, a power of 6 W was used, and the substrate was scribed 1 time. For P3 line, a power of 10 W was used, and the substrate was scribed for 1 time. The widths of P1, P2 and P3 are 150, 500 and 100 μm, respectively. The overall width of a single dead area is 1100 μm. The active area is calculated to be 12.96 cm^2 for a minimodule.

3. Characterization

The top-view and the cross-sectional SEM images were measured by using a Titachi S4800 field-emission scanning electron microscopy (Hitachi High Technologies Corporation). In situ grazing-incidence wide-angle X-ray scattering (GIWAXS) measurements were conducted in a custom-made spin-coater at the BL14B1 beamline of Shanghai Synchrotron Radiation Facility (SSRF). After the perovskite precursor was dropped on the substrate, with the start of the spin coating process, the GIWAXS measurement was triggered simultaneously, which was controlled by a computer program. The grazing incidence angle was 0.4º. The anti-solvent was dripped on the spinning film at 20 seconds, after another 20 seconds, the spinning

process was stopped and the in-situ thermal annealing treatment on the wet film was started immediately. Raising the temperature from 25 °C to 110 °C with 20 seconds. The GIWAXS data was collected every 2 seconds synchronously from 0 s to 400 s. The XRD patterns of the perovskite films were recorded on Bruker D8 advance with a Cu Kα radiation (40 kV, 40 mA) and a scanning rate of 5 °/min in the 2θ range of 5-50° at a step size of 0.02 s. AFM was recorded from Bruker Innova atomic microscopy. KPFM measurements were using BRUKER ICON under a Peak Force KPFM mode, the probe type was SCM-PIT-V2 and the scan rate was 0.5 Hz during the testing process. The samples were scanned in at least three random locations to ensure reliable results. The UV-Visible absorption spectra of the solution and thin films were measured from the absorbance model (without integrating sphere) using PerkinElmer Lambda 950 UV−vis spectrophotometer with a scanning rate of 600 nm/min in the range of 900-300 nm at a step bandwidth of 1 nm. The type of baseline calibration was the 100% transmittance baseline. The viscosity of different perovskite precursors was measured using Anton paar MCR92. The water contact angles on different substrates were measured by using JC2000D2H. Monochromatic external quantum efficiency (EQE) spectra were recorded as functions of wavelength with a monochromatic incident light of 1 x 10^{16} photons cm^{-2} in alternating current mode with a bias voltage of 0 V (Enlitech QE-R3011). The light intensity of the solar simulator was calibrated by a standard silicon solar cell provided by PV Measurements. High-sensitive external quantum efficiency (HS-EQE) for both samples were recorded using Enlitech PECT-600 to extract the Urbach energy (E_U). Electrochemical impedance spectroscopy (EIS) was obtained by using a potentiometer (CHI604E, CH instrument) under dark conditions in the frequency range from 1 MHz to 10 mHz with an AC amplitude of 5 mV. A Fourier transform infrared spectroscopy (FT-IR, Thermo Fisher Nicolet Is5) was used to collect the FT-IR spectral data for the samples without and with MMS-treatment. The liquid state ^1H nuclear magnetic resonance (NMR) measurements were recorded on JNM-ECZ400S/L1 spectrometer (TMS as an internal standard (δ = 0)). UPS and XPS spectra were recorded by a Thermo-Fisher ESCALAB Xi+ system. For XPS measurement, radiation was produced by a monochromatic 75 W Al Kα excitation centered at 1486.7 eV. For UPS measurement, He I ultraviolet radiation source of 21.22 eV was used. The TPC and TPV curves for both devices are detected by Fluxim Paios Spectrometer. The depth profile of the perovskite film on the ITO substrate was recorded using ToF-SIMS (model ION ToF-SIMS 5) with negative polarity. The pulsed primary Bi^+ ion source was operated at 30 keV and 1 pA on a 100*100 μm^2 area to bombard the sample surface to produce secondary ions. The sputtering was performed with a Cs ion beam operated at 0.5

keV and 26 nA on a 300*300 μm^2 area. The colloidal size for different perovskite precursors were measured by using Zeta potential and nanoparticle size analyzer (Malvern Zetasizer Nano ZS90). Viscosity is detected by advanced rotary rheometer MCR92. Hall effect measurement was characterized by Lake shore Accent HL5500 Hall System. A magnetic field (B) (0-0.5 T) perpendicular to the sample surface was applied, and the test current range from -200 mA to 200 mA was applied using Keithley Model 2400. The samples were prepared by depositing a perovskite film on glass substrate (1 × 1 cm^2), which contained two indium electrodes (the distance between the two electrodes is 0.8 cm) depositing on the perovskite film for measurement.

The current-voltage characteristics were measured by Keithley 2400 source and the solar simulator with standard AM 1.5G (100 mW/cm^2, SAN EI: Japan) under ambient conditions. The light intensity was calibrated by a Newport-calibrated standard silicon solar cell. The *J-V* curves were measured by forward (-0.1 V to 1.5 V forward bias) or reverse (1.5 V to -0.1 V) scans with a voltage step of 20 mV and a delay time of 100 ms for each point. The active area of a PSC is 0.12 cm^2. The *J-V* curves for all small sized devices were obtained by masking the cell with a metal mask of 0.09 cm^2 in area.

The unencapsulated devices for long-term stability measurement were stored in a N_2-filled glovebox under dark (temperature is about 25 ^{o}C). After various periods of time, the *J-V* measurements were performed.

The unencapsulated devices for thermal aging evaluation were placed under an 85 ^{o}C hotplate in a N_2-filled glovebox. After various periods of time, the *J-V* curves were collected.

The dynamic MPP tracking of the unencapsulated devices were carried out in a home-made N_2-filled box under 1 sun continuous illumination (white light LED array) with temperature of 30 ± 5 ^{o}C (Multi-Channels Solar Cells Stability Test System, Wuhan 91PVKSolar Technology Co. Ltd, China). The MPPT was automatically recalculated every 2 h by tracking the *J-V* curve.

4. Supplementary Notes

Note S1. Grazing-incidence X-ray diffraction (GIXRD) measurement

GIXRD measurements were using Rigaku Smartlab 3kw. We estimate the stresses of different perovskite films by the GIXRD technique with the 2θ–sin2ψ method and the grazing incidence angle was 1.2^o. Generally, the residual stress can be reflected by the slope of linear fitted 2θ–sin2ψ and the perovskite film stress (σ) can be calculated according to the following equation (equation 1):[1, 2]

$$\sigma = -\frac{E}{2(1+v)}\frac{\pi}{180}\cot\theta_0\frac{\partial(2\theta)}{\partial(sin^2\psi)} \quad (1)$$

Where E and ν are Young's modulus and Poisson's ratio for perovskite films, respectively. θ_0 is the diffraction peak for a stress-free perovskite crystal plane. θ is the diffraction peak for the measured perovskite thin films. ψ is the angle of the diffraction vector with respect to the sample normal direction. The (012) plane is chosen for further analysis due to its high diffraction angle and multiplicative factor, providing the reliable alleviate orientation effect and structure symmetrical information. The 2θ values are linked with the varied instrument tilt angle ψ of 10°, 20°, 30°, 40° and 50° to obtain the corresponding XRD patterns.

Note S2. PL and TRPL measurement

The steady PL spectra and time-resolved PL decay measurements were performed using an FLS980 Series of Fluorescence Spectrometers. For the PL measurement, the excitation source was a monochromatized Xe lamp (peak wavelength at 500 nm with a line width of 2 nm). For TRPL, the excitation source was a supercontinuum pulsed laser sources (YSL SC-PRO) with an excitation wavelength at 800 nm and a repetition rate of 0.1 MHz. The TRPL decay curves were fitted using a bi-exponential function (equation 2) and the fitted data were summarized in Table S2.

$$f(t) = A_1 exp^{(-\frac{t}{\tau_1})} + A_2 exp^{(-\frac{t}{\tau_2})} + B \quad (2)$$

Where, τ_1 represent the fast decay process related to the bimolecular recombination, and τ_2 is the slow decay process associated with the trap-assisted recombination process of charge-carrier.[3] B is a constant for the baseline offset. A_1 and A_2 are constants, representing the contributions of the fast and slow components, respectively. The average PL decay lifetime was calculated using equation 3:

$$\tau_{ave} = \frac{\sum A_i \tau_i^2}{\sum A_i \tau_i} \quad (3)$$

Note S3. Surface recombination velocity (SRV) and bulk lifetime (τ_{bulk})

We measured the TR-PL lifetime as a function of the thickness of perovskite films to extract SRV and τ_{bulk}. The sample stack is FTO/NiOx/Me-4PACz/perovskite/TOPO. According to previous reports, TOPO (trioctylphosphine oxide, 10 mg mL^{-1} in chlorobenzene) is an effective passivation on the top surface. Following a double-

heterostructure model, the perovskite film thickness d is below 1 μm, much shorter than the carrier diffusion length, so that surface recombination in surface and bulk can be simultaneously probed. The effective lifetime (τ_{eff}) is related to the bulk lifetime (τ_{bulk}) and surface lifetime (τ_s), and calculated using a stretched exponential fitting:[4, 5]

$$\frac{1}{\tau_{eff}} = \frac{1}{\tau_{bulk}} + \frac{1}{\tau_s} = \frac{1}{\tau_{bulk}} + \frac{2SRV}{d} \quad (4)$$

Hence, plotting $\frac{1}{\tau_{eff}}$ against $\frac{2}{d}$ yields a straight fitted line where the intercept is $\frac{1}{\tau_b}$, and the slope is SRV. The decay curves were shown in Fig. S21.

Note S4. SCLC measurement

The electron-only or hole-only devices were assembled for the SCLC measurement. The dark I-V curves of the electron-only and hole-only devices can be divided into three parts: Ohmic region, trap-filling limited region with a sharp increase in current and the trap-free Child's region. The trap density, n_t, can be determined using equation 5.[6]

$$V_{TFL} = \frac{en_tL^2}{2\varepsilon\varepsilon_0} \quad (5)$$

Where, V_{TFL} is the trap-filled limit voltage, n_t is the trap density, L is the thickness of perovskite film, ε is the relative dielectric constant of the perovskite, [7] and ε_0 is the vacuum permittivity. To maximize the accuracy of the results, we first fabricated the device with completely symmetric structures (PCBM/PCBM for the electron-only device, PTAA/PTAA for the hole-only device). Secondly, we adopted a fast scan rate to preclude the influence of mobile ion.[8] Thirdly, a forward scan was used due to the steady-state output efficiency approaching the forward scan efficiency. Fourthly, we selected the V_2 as the intersection point to calculate the trap-state density.[9]

Note S5. EQE of EL

The EL spectra of both devices were recorded by a light emitting diode PL quantum-yield measurement system equipped with Enlitech REPS-VOC Source Measurement Unit. The voltage deficit ($V_{loss}^{non-rad}$) related to the non-radiative recombination was calculated using the following equation: [5, 10, 11]

$$V_{loss}^{non-rad} = -\frac{k_BT}{q}\ln(EQE_{EL}) \quad (6)$$

Where k_B is the Boltzmann constant, T is absolute temperature, q is the elementary charge, EQE_{EL} is the EQE value of the device working as LED under the injection current equal to that of the J_{SC} of the solar cell.

Note S6. Stability test energy yield (STEY) and degradation rate (DR)

The stability test energy yield (STEY) and degradation rate (DR) can be calculated according to the following equations:[12, 13]

$$E_{\Delta\tau} = \int_0^{\Delta\tau} P_{out} dt = \int_0^{\Delta\tau} P_{in} PCE dt \quad (7)$$

Where $\Delta\tau$, operational stability test time; $E_{\Delta\tau}$, operational stability test energy yield (STEY) for a test of duration $\Delta\tau$; t, time; STEY is taken for 200 h and 1000 h of stability tests as E_{200h} and E_{1000h}, respectively.

$$DR_{\Delta\tau} = \frac{PCE(\tau) - PCE(0)}{\Delta\tau} \quad (8)$$

$DR_{\Delta\tau}$, effective overall degradation rate for an operational stability test of duration $\Delta\tau$; DR_{200h} and DR_{1000h} are taken as the overall degradation rates for 200 h and 1000 h of stability tests, respectively.

5. Supplementary Figures

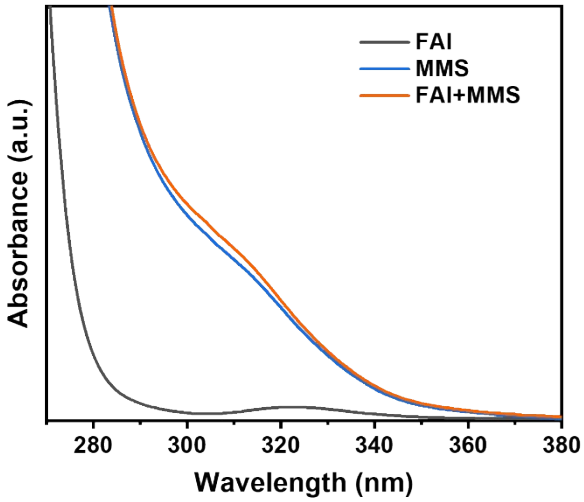

Fig. S1. UV-Vis absorption spectra of MMS, FAI, and MMS+FAI solution (solvent: DMSO).

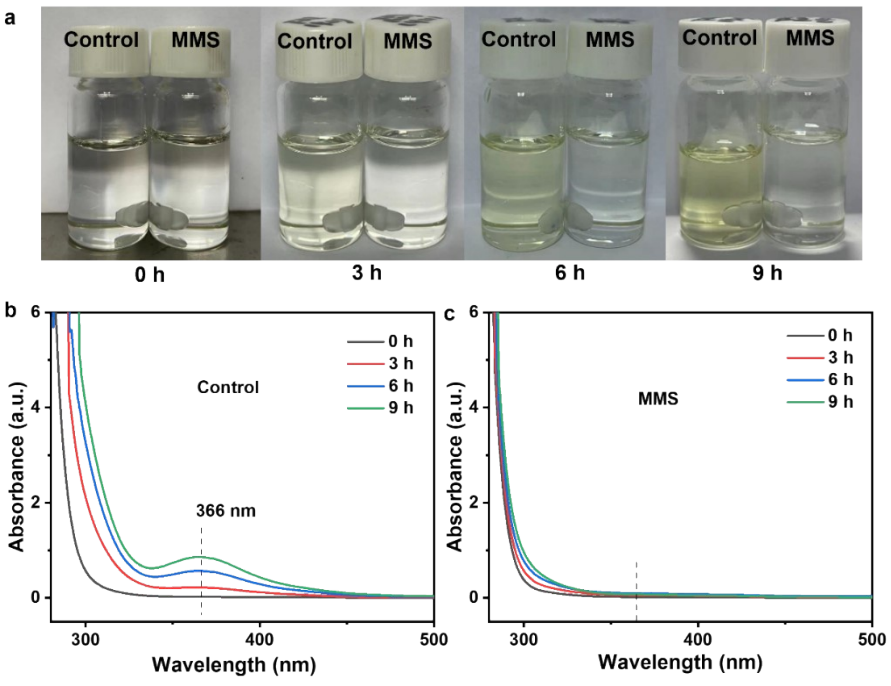

Fig. S2. The photographs (a) and UV-Vis absorption spectra for (b) the control (FAI/DMF solution, 100 mg/mL) and (c) the MMS-containing samples (FAI/DMF solution with 10 μL/mL MMS stabilizer), aged at 50 °C. The control sample degrades (transparent colorless solution turns yellow), associated with a continuously increased intensity of absorbance peak at 366 nm. In contrast, there are almost no changes in the color and absorption spectra for the MMS-containing sample.

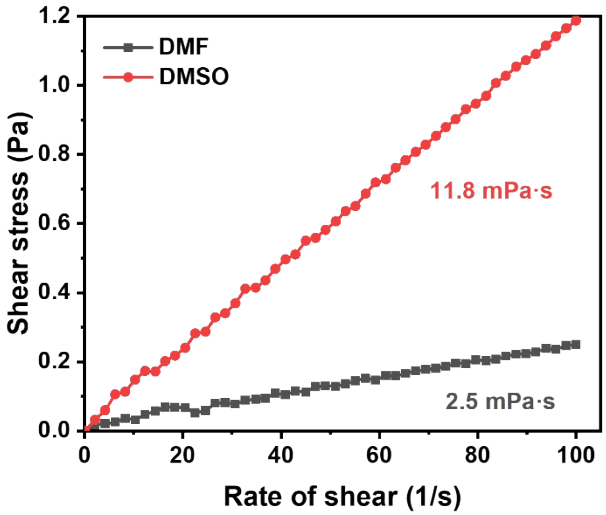

Fig. S3. Viscosity of perovskite precursor with net DMF and DMSO as the solvent.

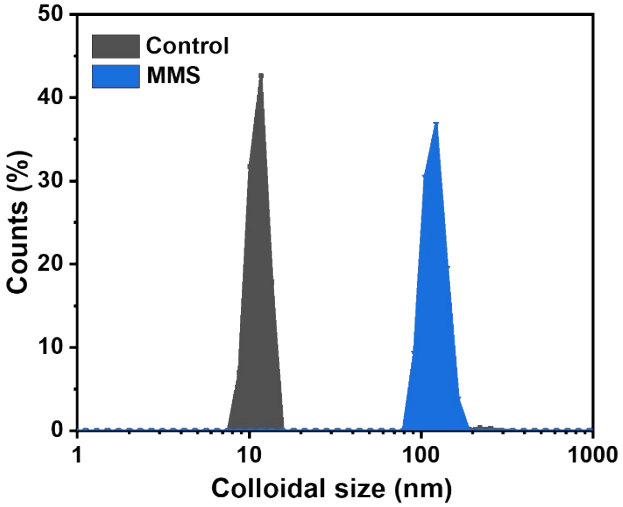

Fig. S4. The colloidal size of the control and MMS-containing precursor solutions detected by dynamic light scattering (DLS).

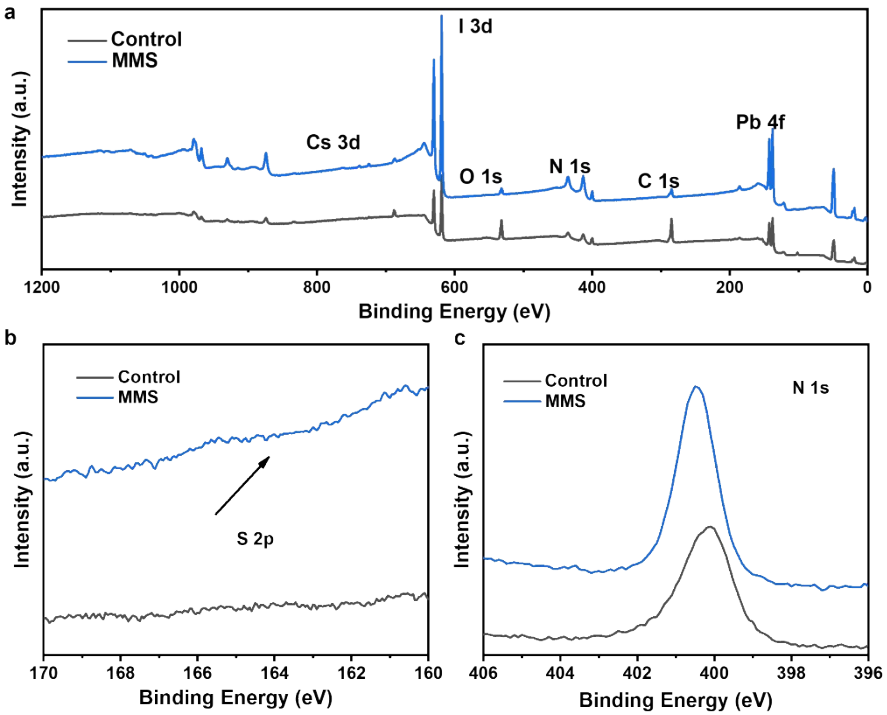

Fig. S5. XPS spectra of the control and MMS treated perovskite films: (a) survey, high resolution spectra of (b) S 2p, and (c) N 1s.

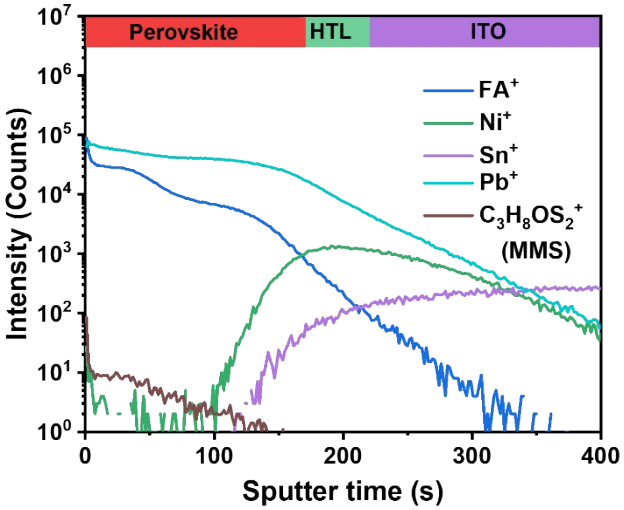

Fig. S6. ToF-SIMS profiles for the MMS-treated films (ITO/NiOx/SAM/perovskite).

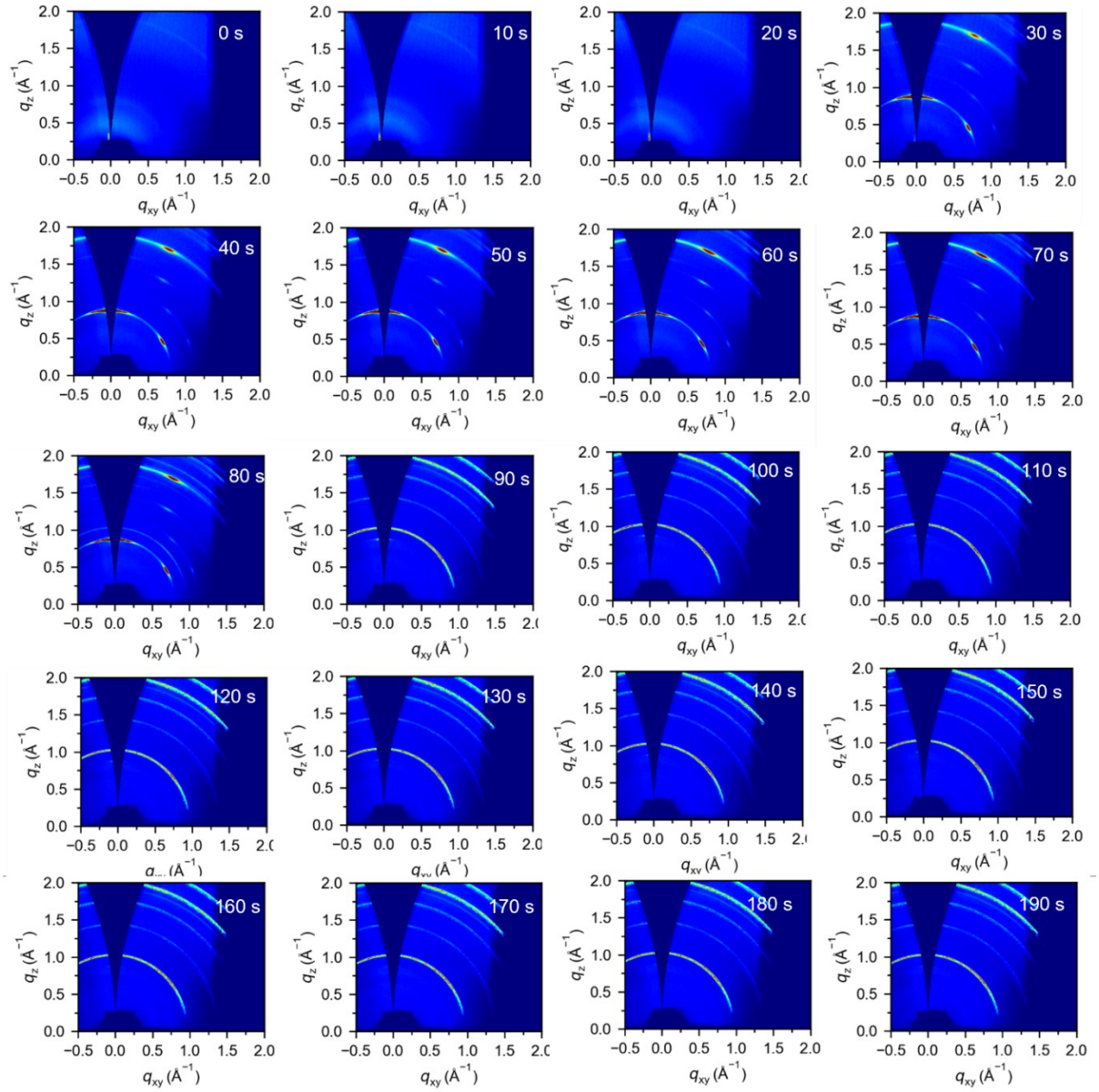

Fig. S7. Time evolution (10 s/frame) of GIWAXS patterns for the control sample upon anti-solvent dripping and thermal annealing.

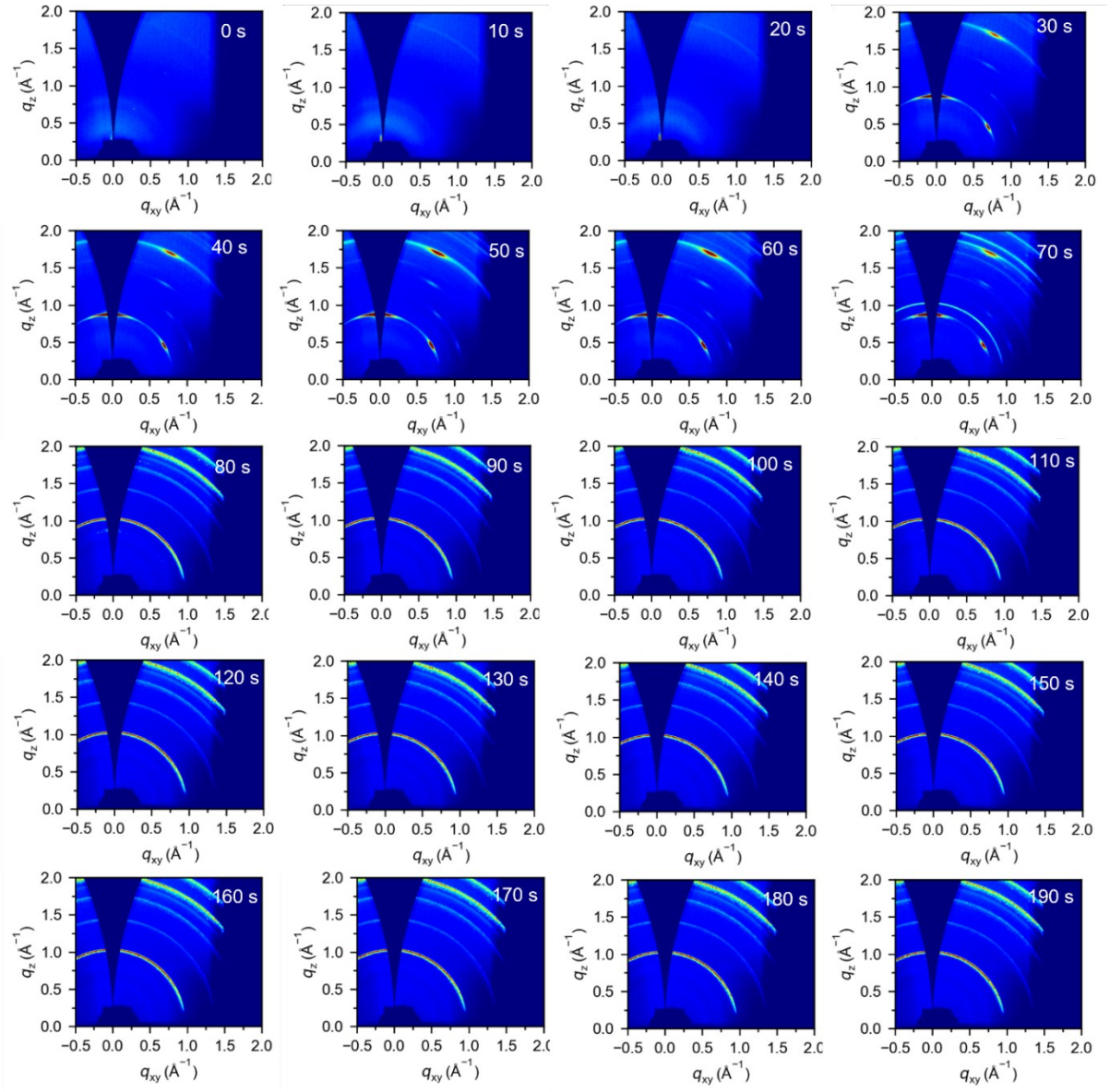

Fig. S8. Time evolution (10 s/frame) of GIWAXS patterns for the MMS-treated sample upon anti-solvent dripping and thermal annealing.

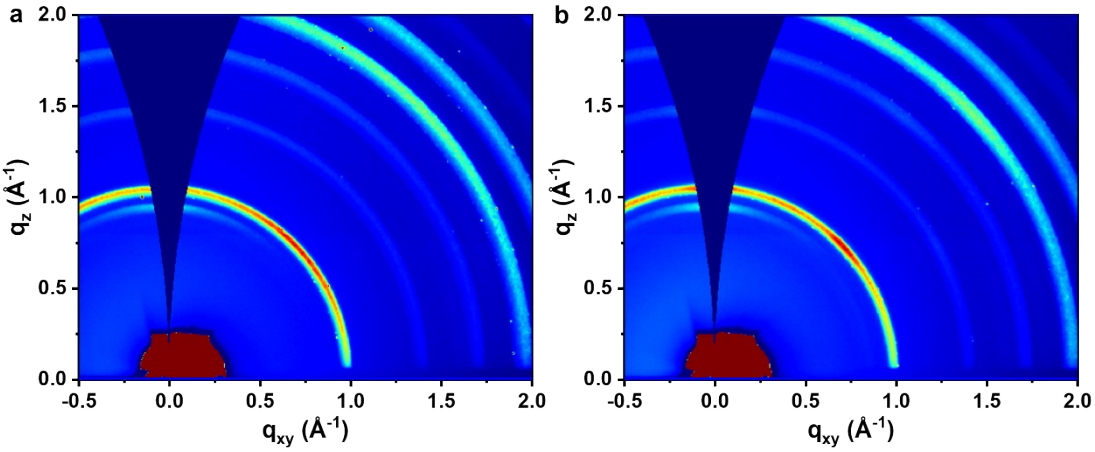

Fig. S9. GIWAXS patterns of the final (a) control and (b) MMS-based perovskite films.

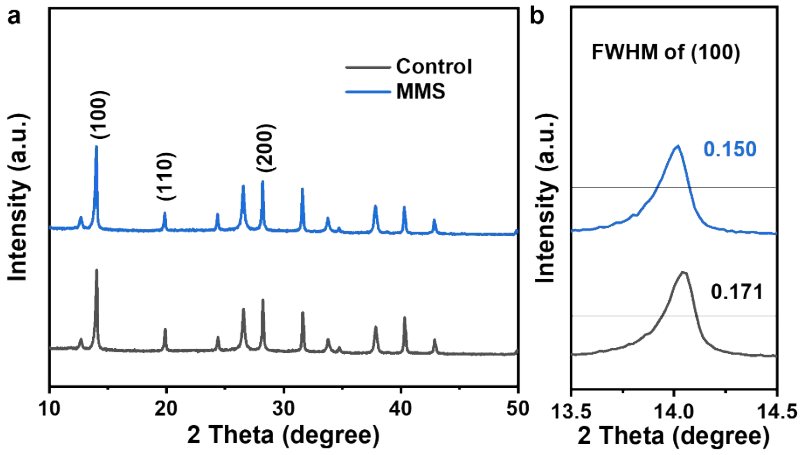

Fig. S10. (a) XRD patterns of the control and MMS-treated perovskite films and (b) the partial enlarged XRD for the (100) crystal facet.

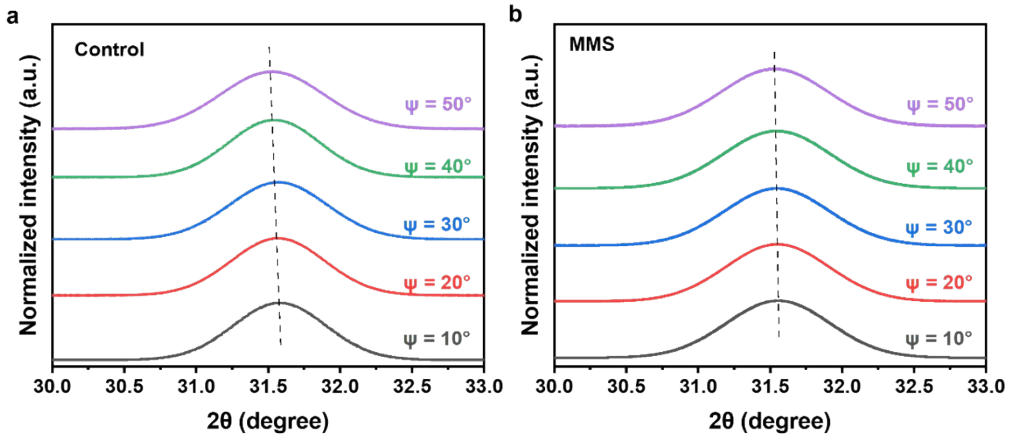

Fig. S11. Grazing incidence x-ray diffraction (GIXRD) of the (a) control and (b) MMS-treated perovskite films vary with ψ from 10 to 50° (the grazing incident angle is 1.2°).

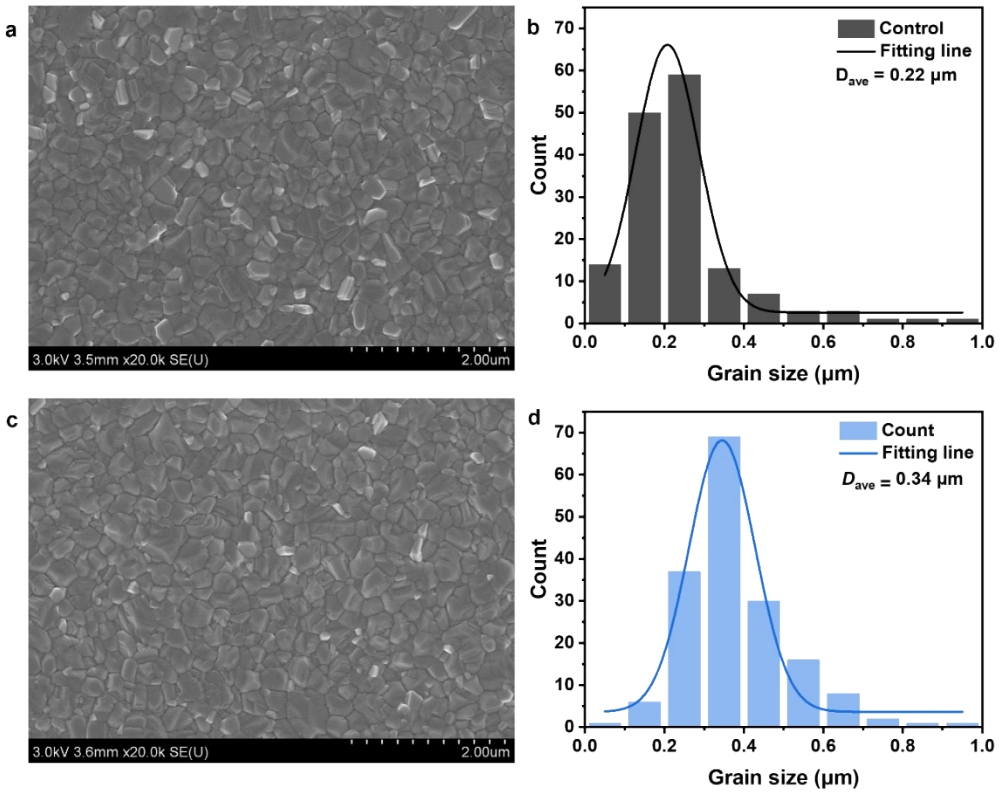

Fig. S12. SEM images and the corresponding grain size distributions of (a,b) the control and (c,d) MMS-treated perovskite films.

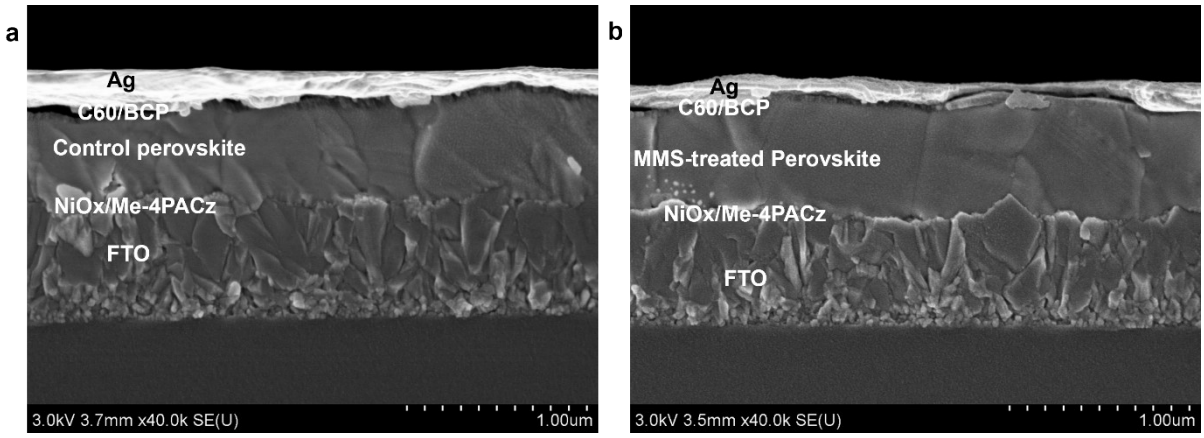

Fig. S13. The cross-sectional SEM images of (a) the control and (b) MMS-based devices.

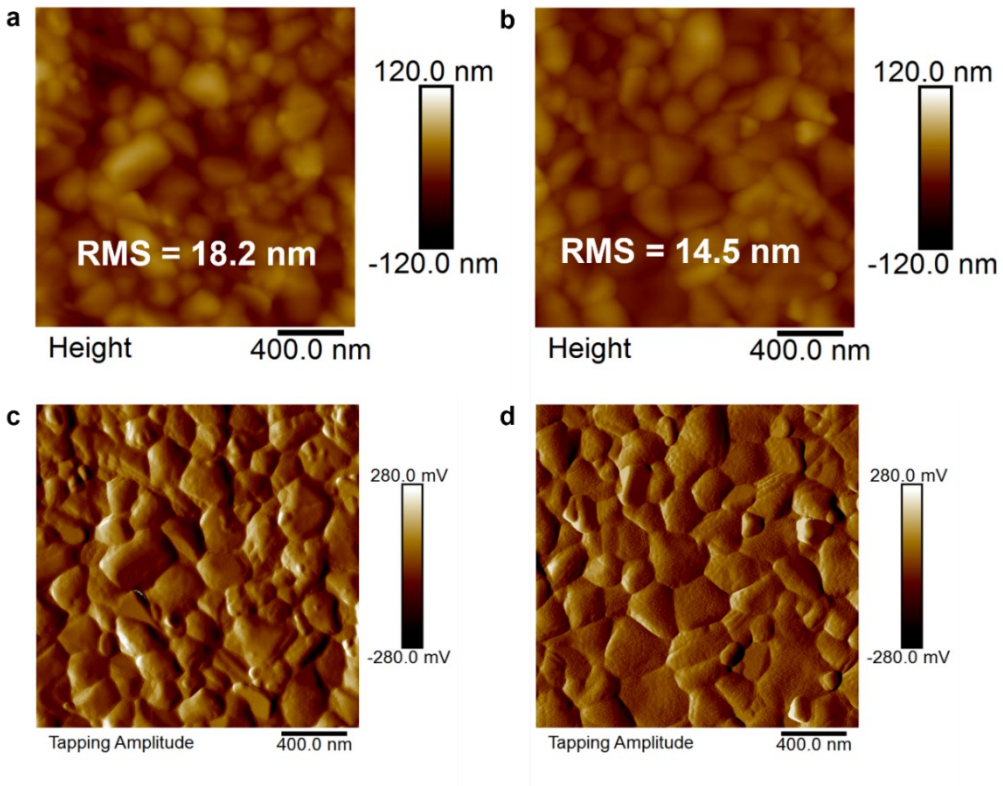

Fig. S14. AFM images and the corresponding amplitude for (a,c) the control and (b,d) the MMS-treated perovskite films.

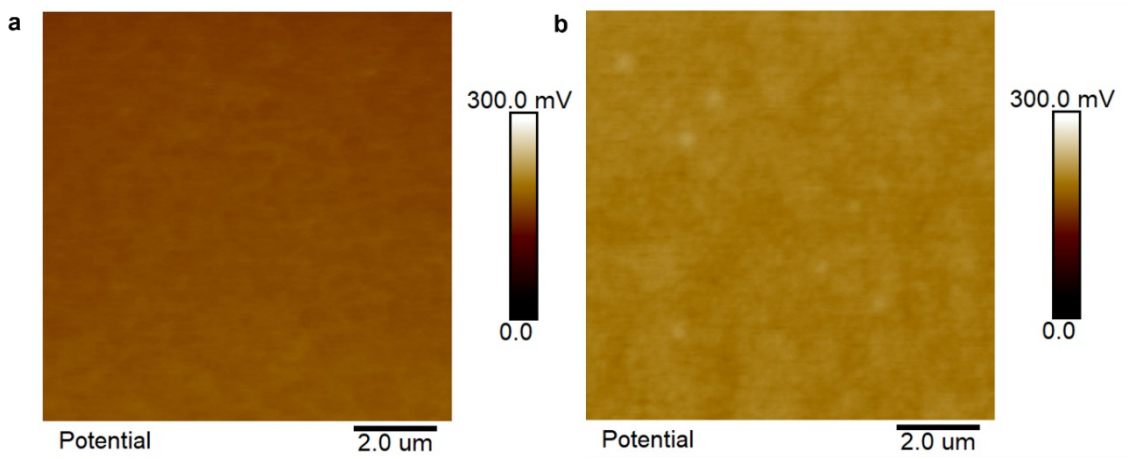

Fig. S15. Surface contact potential mapping of (a) the control and (b) MMS-treated perovskite films measured by using Kelvin probe force microscopy (KPFM).

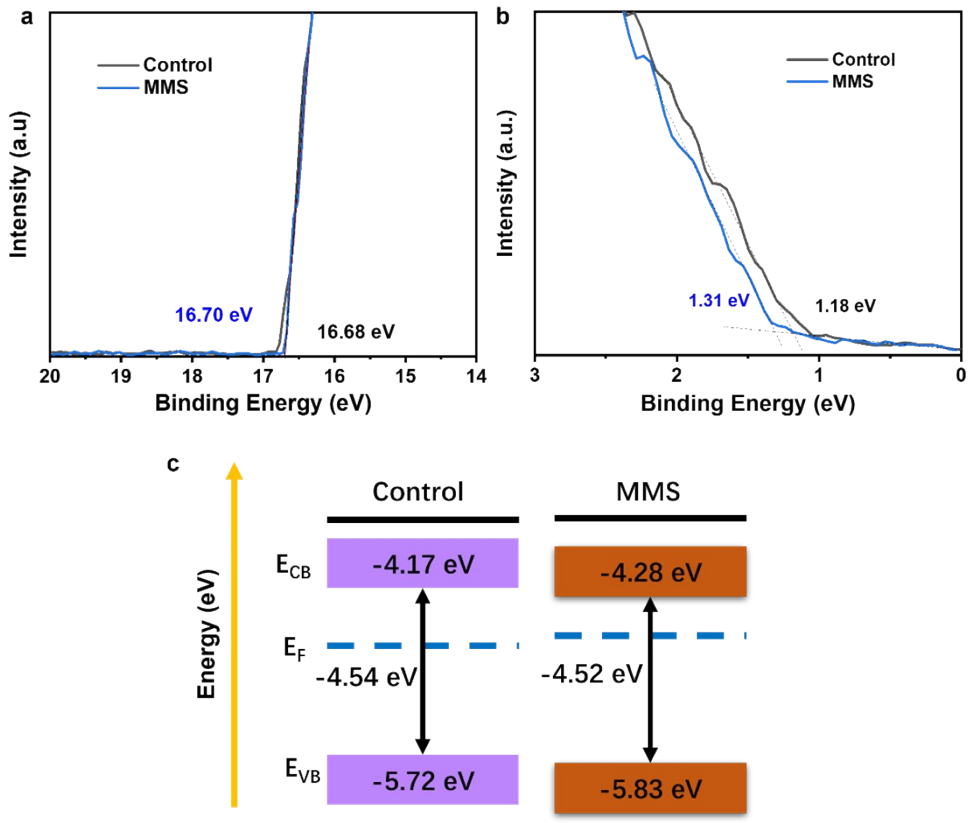

Fig. S16. UPS spectra of (a) the control and (b) the MMS-treated perovskite films. (c) The corresponding energy levels.

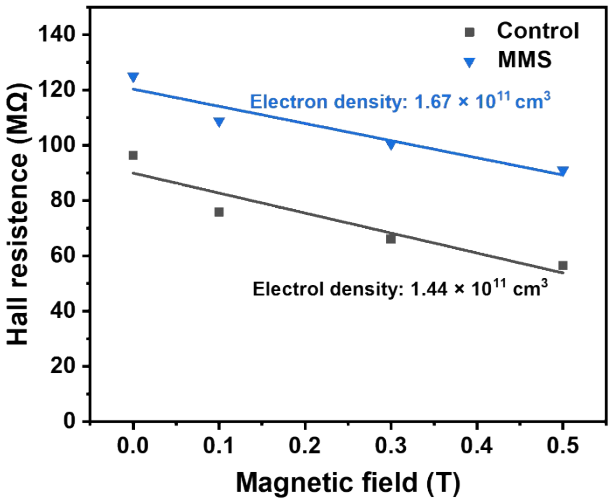

Fig. S17. Hall effect measurement of perovskite films without and with MMS treatment.

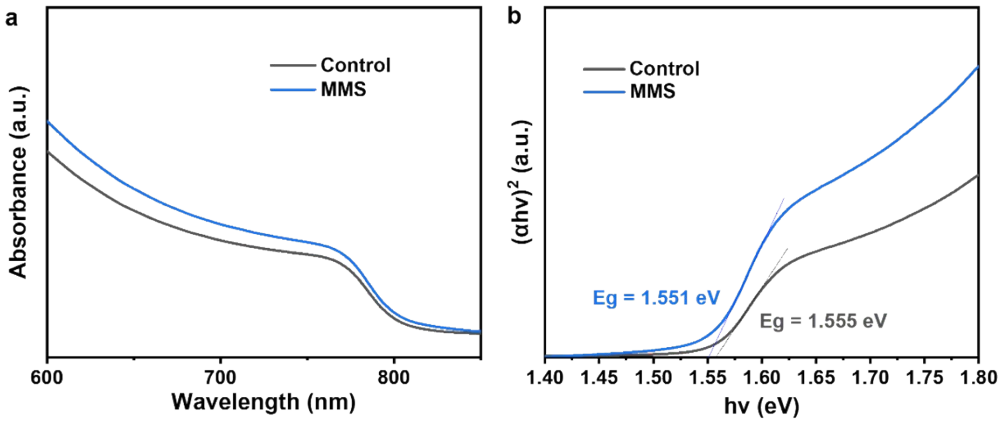

Fig. S18. (a) UV-Vis absorption spectra and (b) the corresponding bandgaps of the control and MMS-treated perovskite films.

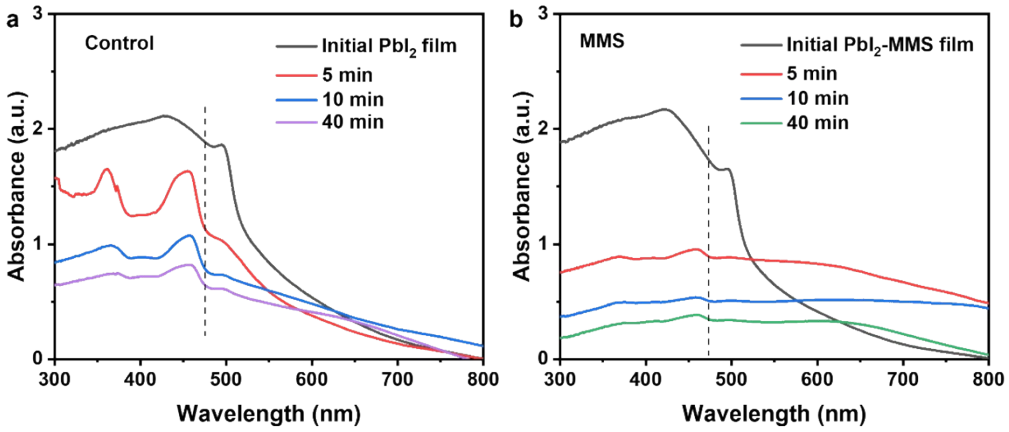

Fig. S19. UV-vis absorption spectra of (a) PbI_2 films and (b) PbI_2-MMS films immersed in FAI/IPA for different time scales. For all the initial films, 5 mol.% of CsI was added to assist the phase transformation. The absorption threshold at 470 nm corresponds to the absorption of δ-$FAPbI_3$.

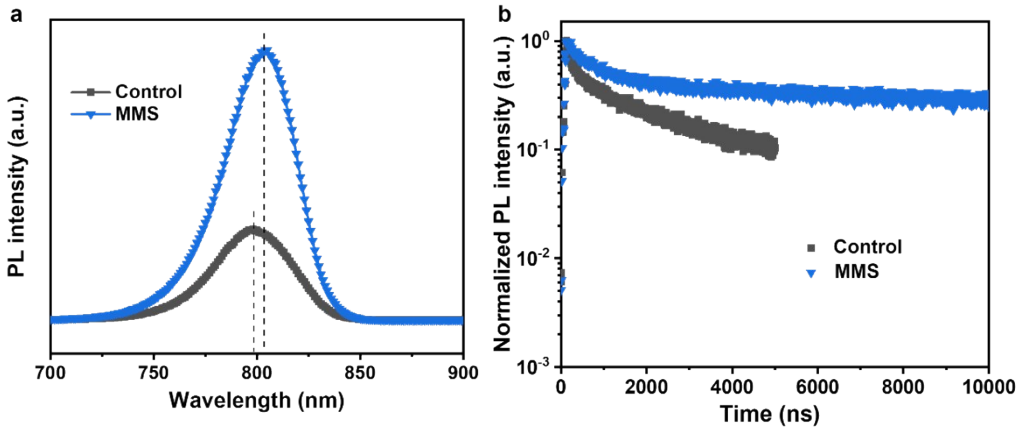

Fig. S20. (a) The steady-state photoluminescence (PL) and (b) time-resolved photoluminescence (TR-PL) spectra of the control and MMS-treated perovskite films.

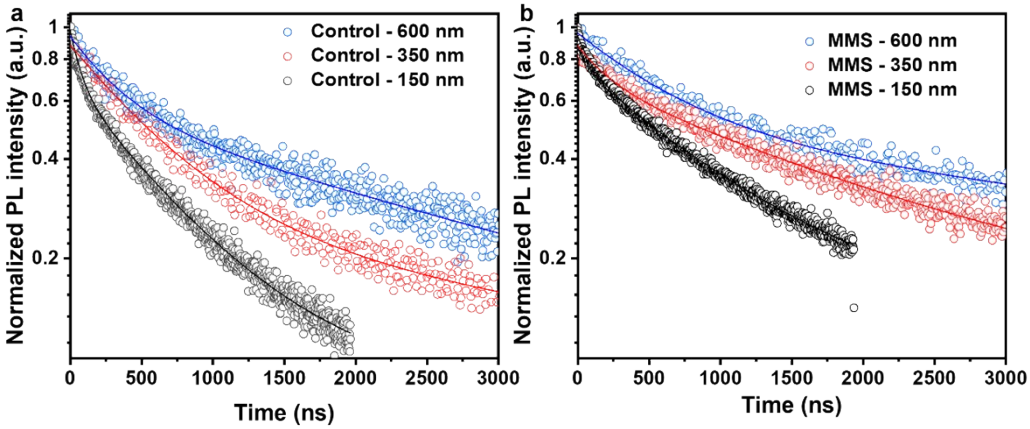

Fig. S21. The time-resolved photoluminescence (TR-PL) spectra of (a) the control and (b) MMS-treated perovskite films with different thicknesses.

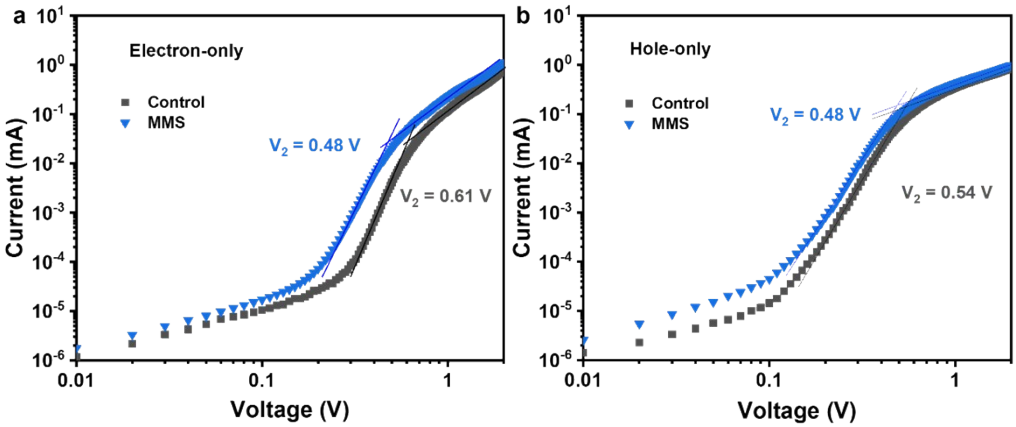

Fig. S22. Dark current-voltage curves for (a) the electron-only structured devices (FTO/PCBM/Perovskite/PCBM/BCP/Ag) and (b) the hole-only devices (FTO/PTAA/Perovskite/PTAA/Ag) based on the control and MMS-treated perovskites.

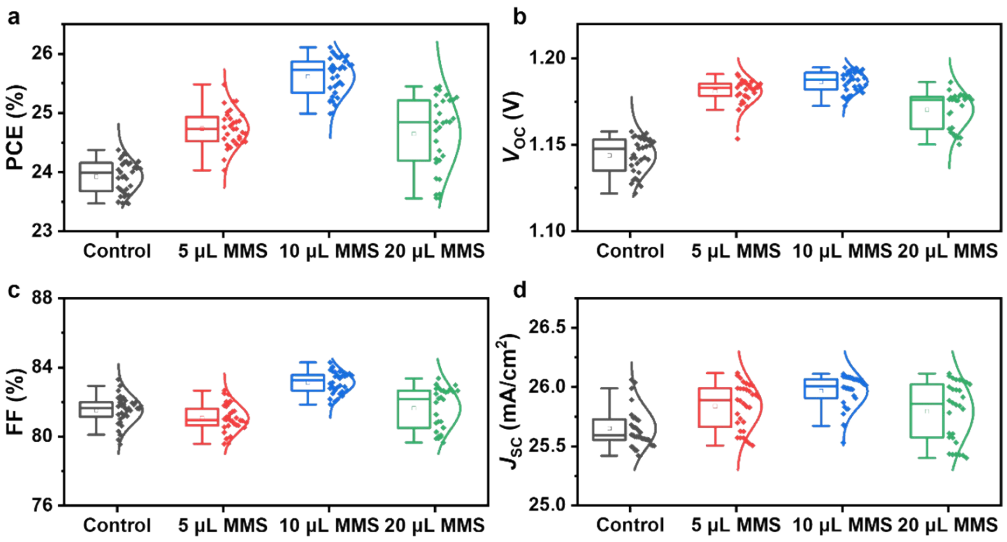

Fig. S23. Statistics of the PV parameters for devices with different concentrations of MMS. (a) PCE, (b) V_{OC}, (c) FF, and (d) J_{SC}.

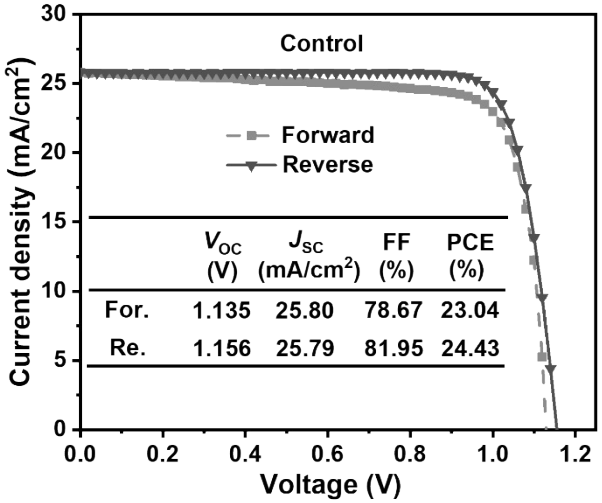

Fig. S24. *J-V* curves of the champion control device from reverse and forward scans.

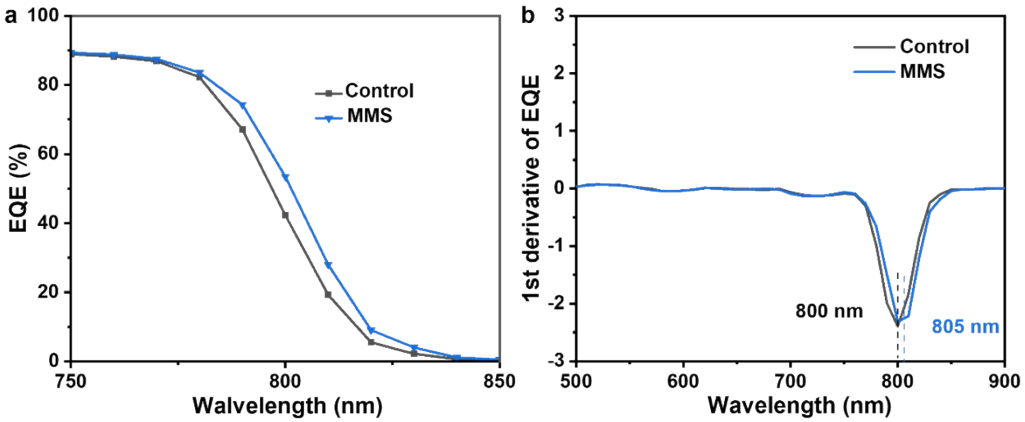

Fig. S25. (a) Partial enlarged EQE spectra and (b) 1st derivative of the EQE for the control and MMS-based devices.

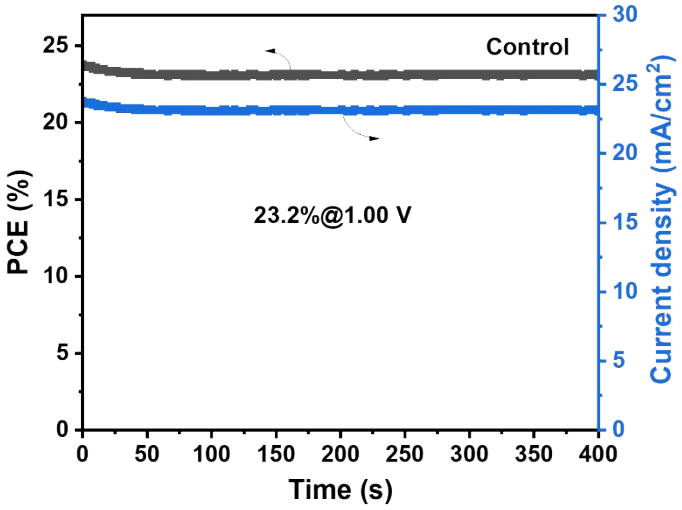

Fig. S26. Stabilized output efficiency of the control device around the maximum output power point as a function of time under simulated 1 sun illumination.

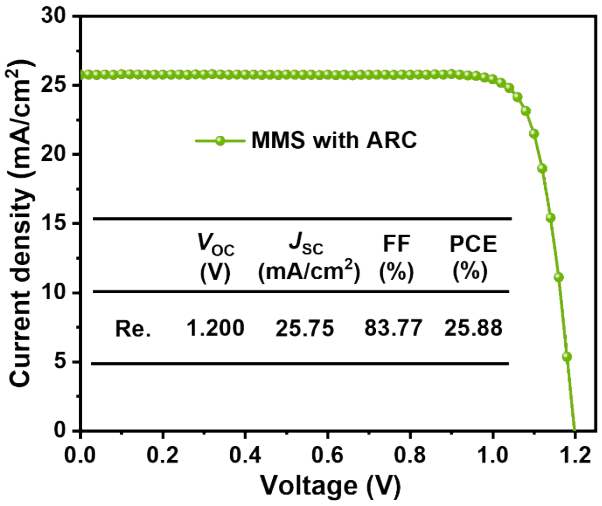

Fig. S27. *J-V* curve of the MMS-based device with the highest V_{OC}.

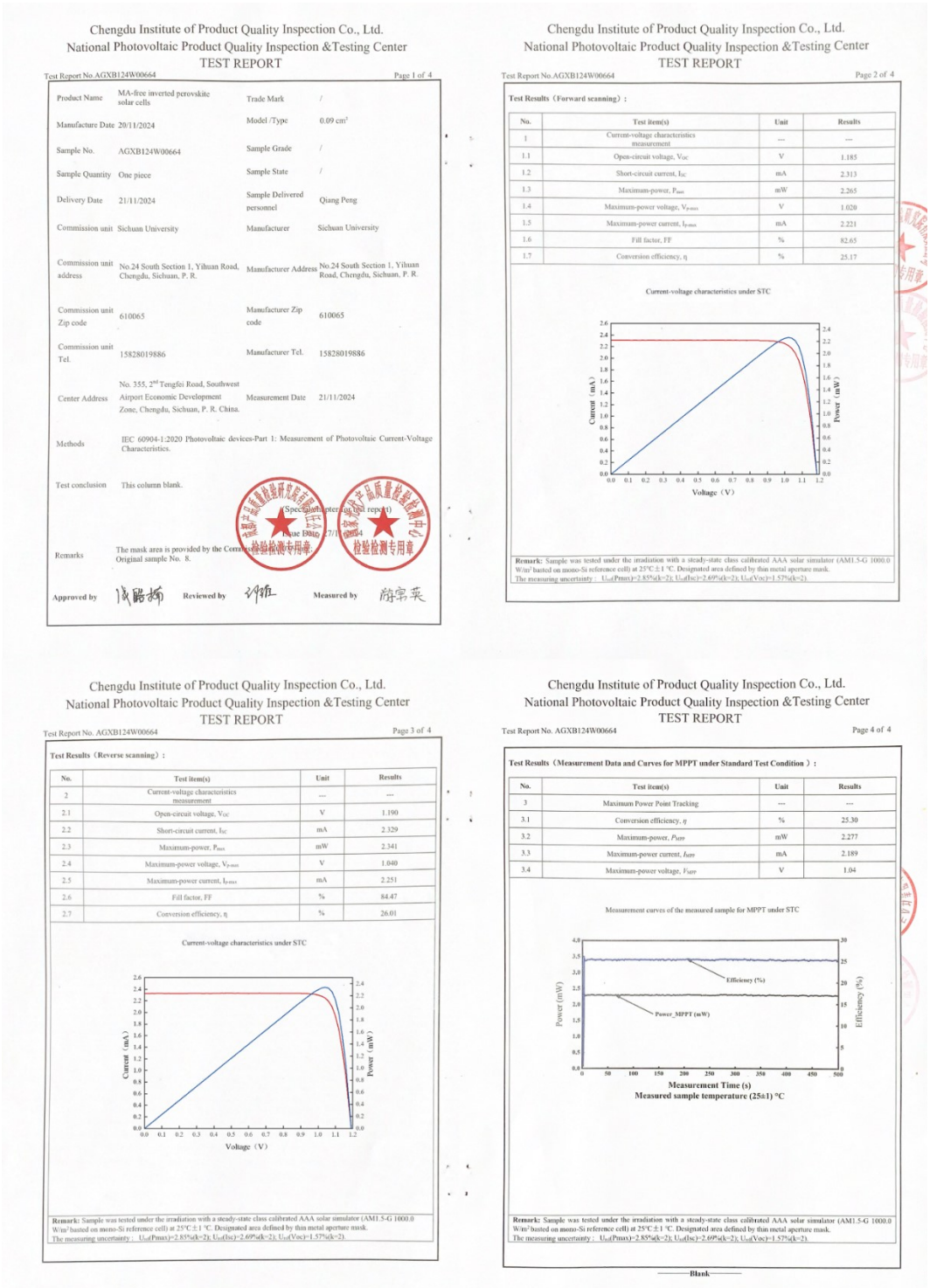

Fig. S28. The certification report of photovoltaic performance for the MMS-based perovskite solar cell (aperture area: 0.09 cm^2) with forward and reverse scan and a quasi-steady-state output efficiency from National Photovoltaic Product Quality Inspection & Testing Center, China.

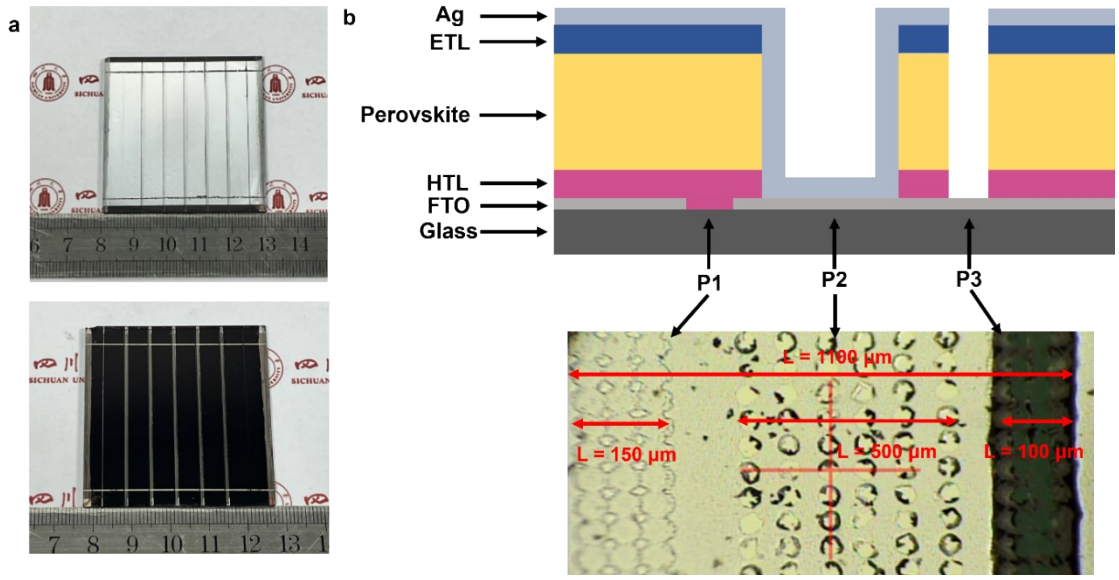

Fig. S29. (a) The photographs of the fabricated mini modules. (b) The geometry design for the perovskite minimodule (top) and the microscopy image of minimodule patterns P1, P2 and P3 (bottom).

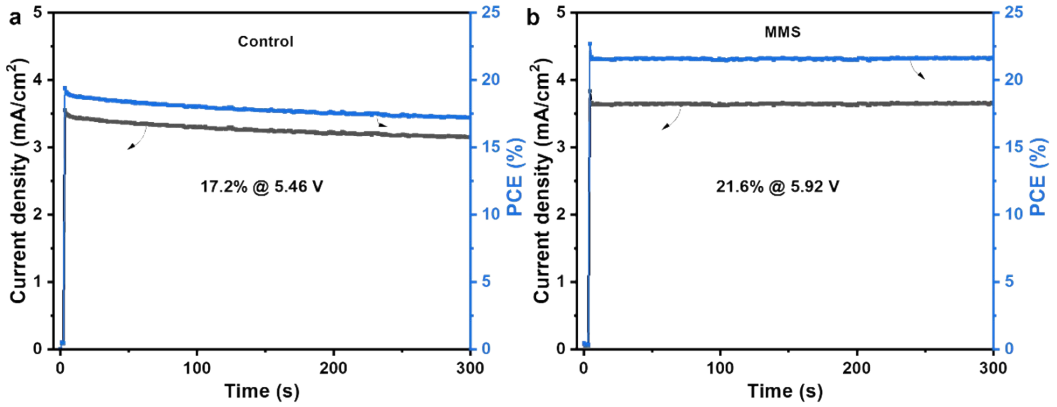

Fig. S30. The steady-state output efficiency of (a) the control and (b) MMS-mediated minimodules around the maximum output power point under standard 1 sun illumination.

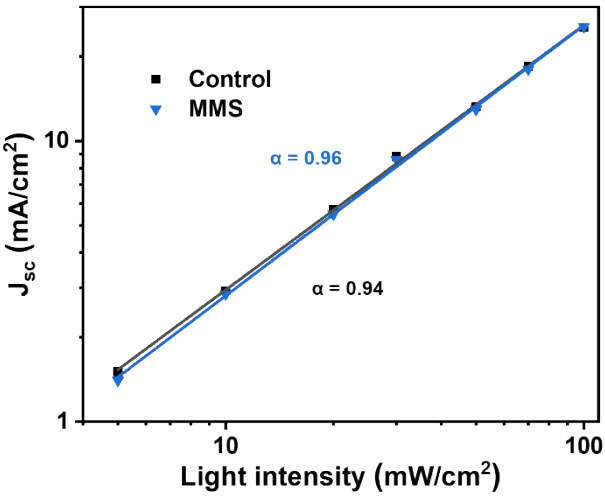

Fig. S31. J_{SC} vs. light intensity for the devices without and with SA-derivative treatment.

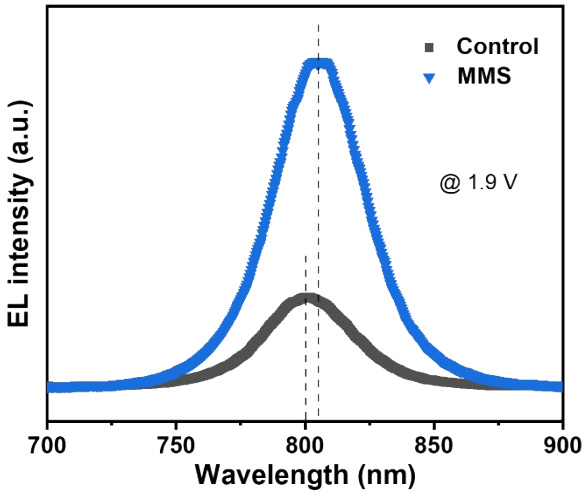

Fig. S32. Electroluminescence (EL) spectra of the control and the MMS-based devices work as a light-emitting diodes under 1.9 V.

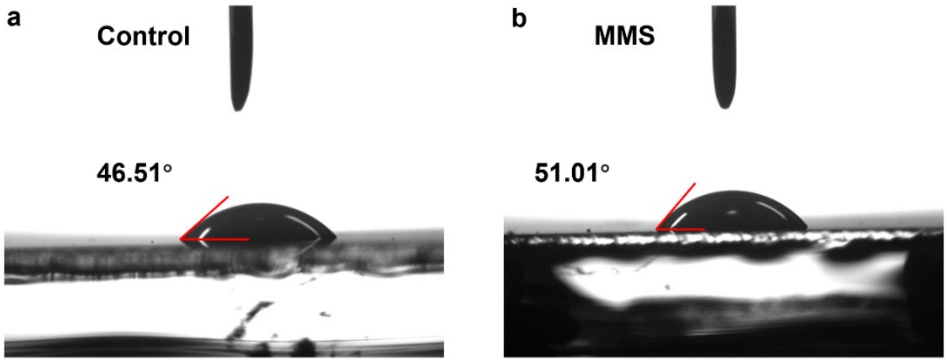

Fig. S33. The water contact angle on (a) the control and (b) MMS-treated perovskite films.

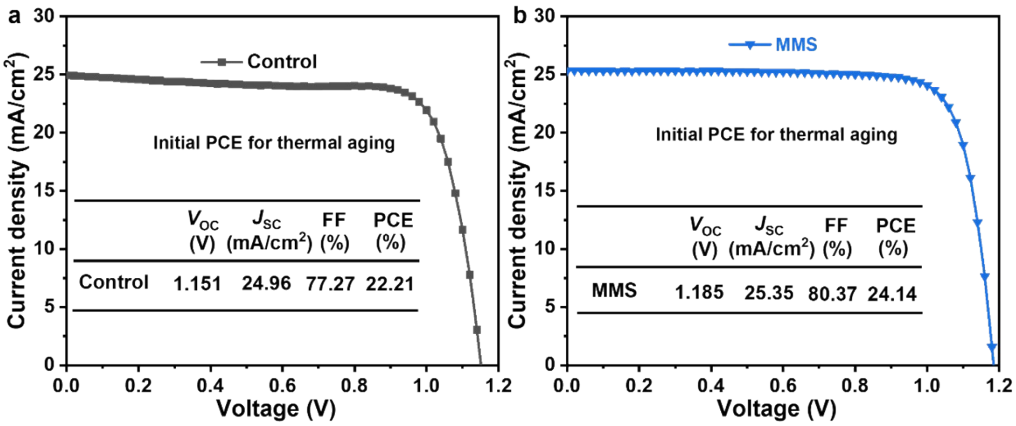

Fig. S34. Initial efficiencies of the control and MMS-treated devices for thermal aging evaluation (placed under 85 °C hotplate in a N_2 filled glovebox).

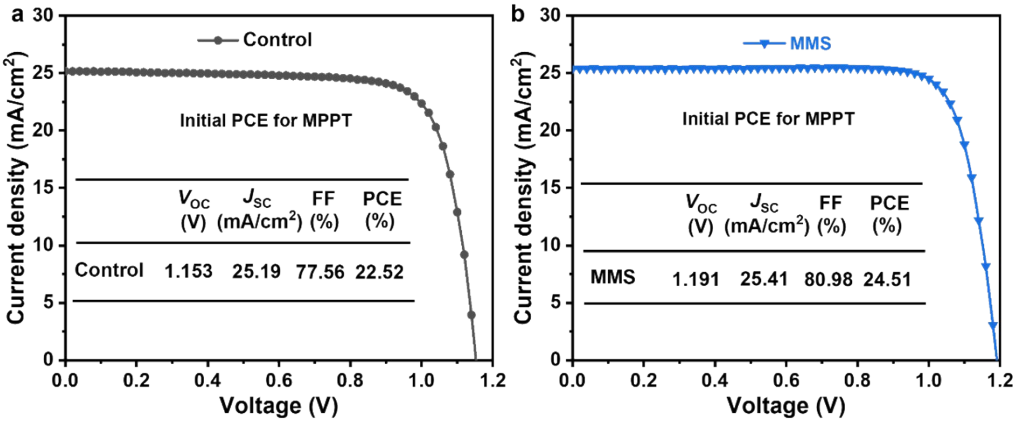

Fig. S35. Initial efficiencies of the control and MMS-treated devices for MPPT measurement.

6. Supplementary Tables

Table S1. Summary of PV parameters for small area inverted PSCs (PCE > 23%) based on MA-free CsFA-based perovskites without MACl additive.

Device Configurations	Eg (eV)	Scan direction	V_{OC} (V)	J_{SC} (mA/cm^2)	FF (%)	PCE (%)	Ref.
ITO/NiOx/PTAA//$FA_{0.95}Cs_{0.15}PbI_3$/PCBM/BCP/Ag.	1.52	Reverse	1.138	25.38	81.40	23.49	14
		Forward	1.140	25.38	80.30	23.25	
ITO/P3CTN/$Cs_{0.05}FA_{0.95}PbI_3$/C_{60}/TPBi/Cu	/	Reverse	1.140	26.30	78.60	23.50	15
		Forward	/	/	/	/	
FTO/SAM/$FA_{0.95}Cs_{0.05}PbI_3$/C_{60}/BCP/Ag	1.52	Reverse	1.150	24.95	82.00	23.53	16
		Forward	1.139	24.77	80.10	22.60	
ITO/p-PY/$FA_{0.98}Cs_{0.02}PbI_3$/PCBM/BCP/Ag	1.55	Reverse	1.176	25.88	82.50	25.10	17
		Forward	1.174	25.84	82.10	24.90	
ITO/NiOx/PTAA/Al_2O_3/$Cs_{0.05}FA_{0.95}PbI_3$/PCBM/BCP/Ag	1.55	Reverse	1.165	26.22	82.20	25.12	18
		Forward	1.167	26.26	81.70	25.03	
ITO/MeO-2PACz/$FA_{0.95}Cs_{0.05}PbI_3$/C_{60}/BCP/Ag (single crystal)	/	Reverse	1.091	28.07	79.30	24.29	19
		Forward	/	/	/	/	
ITO/NiOx/$FA_{0.97}Cs_{0.03}PbI_3$/C60/BCP/Cu	1.54	Reverse	1.125	24.98	83.95	23.60	20
		Forward	/	/	/	/	
FTO/MeO-2PACz/$FA_{0.96}Cs_{0.04}PbI_{2.8}Br_{0.12}$/PCBM/BCP/Ag	/	Reverse	1.170	25.35	81.05	24.14	21
		Forward	1.170	25.37	79.93	23.71	
ITO/NiOx/PTAA/Al_2O_3/$FA_{0.95}Cs_{0.15}PbI_3$/PCBM/BCP/Ag	1.52	Reverse	1.156	25.99	82.11	24.67	22
		Forward	1.153	25.90	81.91	24.46	
ITO/NiOx/PTAA/Al_2O_3/$Cs_{0.05}FA_{0.95}PbI_3$/PCBM/BCP/Ag	1.55	Reverse	1.156	25.96	81.97	24.58	23
		Forward	1.156	25.94	81.27	24.38	
ITO/MeO-2PACz/$FA_{0.91}Cs_{0.09}Pb(I_{0.95}Br_{0.05})_3$/$C_{60}$/BCP/Ag	1.57	Reverse	1.120	25.19	84.76	24.01	24
		Forward	/	/	/	/	
ITO/NiOx/$FA_{0.95}Cs_{0.05}PbI_3$/PCBM/BCP/Ag	1.53	Reverse	1.180	25.91	81.86	25.03	25
		Forward	1.179	25.73	81.19	24.60	
ITO/MeO-2PACz/$FA_{0.95}Cs_{0.05}PbI_3$/C_{60}/BCP/Ag	1.52	Reverse	1.170	25.77	84.02	25.35	26
		Forward	1.170	25.64	83.82	25.08	

FTO/NiO_x/Me-4PACz/$FA_{0.95}Cs_{0.05}PbI_3$/C_{60}/BCP/Ag	**1.55**	**Reverse**	**1.192**	**26.00**	**84.27**	**26.12**	**This Work**
		Forward	**1.184**	**25.95**	**82.69**	**25.41**	

Table S2. Parameters of the TRPL spectroscopies based on different samples.

Samples	τ_{ave} (ns)	τ_1 (ns)	τ_2 (ns)	A_1	A_2
Glass/Control perovskite	1317	116.3	1543.9	1.17	0.47
Glass/MMS-treated perovskite	4106	502.4	5090.1	0.62	0.22

Table S3. Summary on the energy levels for all functional layers used in this study.

Functional layers	HOMO/VBM [eV]	WF [eV]	LUMO/CBM [eV]	Refs.
FTO		-4.7		[27]
NiOx	-5.4		-1.8	[28]
Me-4PACz	-5.6		-1.6	[29]
Control perovskite	-5.72	-4.54	-4.17	
MMS-treated perovskite	-5.83	-4.52	-4.28	
C60	-6.4		-4.5	[30]
BCP	-7		-3.5	[31]
Ag		-4.3		[31]

Table S4. Summary on the output energy for recently published minimodules with similar area.

Area (cm^2)	PCE (%)	Output energy (P_{in}*PCE*Area)	Refs
14.65	21.0	0.31 W	*Science* 2023, **382**, 1399.[32]
9.66	22.0	0.21 W	*Science* 2023, **380**, 404.[33]
17.1	21.4	0.36 W	*Science* 2023, **379**, 288.[34]
16.0	20.0	0.32 W	*Adv. Mater.* 2023, **35**, 2205027.[35]
12.25	18.3	0.22 W	*Joule* 2023, **7**, 1574.[36]
12.7	17.1	0.22 W	*Adv. Energy Mater.* 2023, **13**, 2203898.[37]

18.0	21.16	0.38 W	*Angew. Chem., Int. Ed.* 2024, **63**, e202409689.[38]
12.4	23.34	0.29 W	*Joule* 2024, **8**, 2539.[39]
7.20	21.4	0.15 W	*Nature* 2024, DOI: 10.1038/s41586-024-08159-5.[40]
13.44	23.60	0.32 W	*Nat. Energy* 2024, DOI: 10.1038/s41560-024-01667-8.[41]
12.96	**22.67**	**0.29 W**	**This work**

Table S5. EIS parameters of the devices based on the control and MMS-treated perovskite films.

Devices	R_{rec} (ohm)	CPE (F)
Control	8.373×10^6	7.325×10^{-9}
MMS	9.464×10^6	7.355×10^{-9}

Table S6. Time evolution of the PV parameters for PSCs without and with MMS treatment.

Devices	Time (h)	V_{OC} (V)	J_{SC} (mA/cm^2)	FF (%)	PCE (%)
Control	0	1.159	25.13	80.33	23.39
	24	1.159	25.11	80.60	23.45
	360	1.158	24.76	79.61	22.83
	552	1.146	24.69	78.92	22.32
	960	1.124	24.21	79.28	21.57
	1224	1.125	24.01	76.01	20.53
MMS-based device	0	1.177	25.51	84.57	25.40
	24	1.167	25.48	84.65	25.17
	360	1.169	25.40	83.57	24.81
	552	1.166	25.42	83.04	24.61
	960	1.164	25.42	83.47	24.68
	1224	1.171	25.21	82.85	24.45
	1630	1.176	25.38	82.56	24.63
	2184	1.174	25.20	83.56	24.72

Table S7. Summary on the stability test energy yield (STEY) and degradation rate (DR) for recently published work.

E_g (eV)	0 h PCE (%)	200 h PCE (%)	1000 h PCE (%)	E_{200h} (Wh cm^{-2})	E_{1000h} (Wh cm^{-2})	DR_{200h} (day^{-1})	DR_{1000h} ($week^{-1}$)	Comments	Refs.
1.53	19.8	16.0	12.9	3.5	14.7	-0.47%	-1.15%	MPP, AM1.5G, N_2, 45°C	*Adv. Funct. Mater.*, 2023, **33**, 2213961.[42]
1.53	22.9	23.1	23.4	4.6	23.3	+0.02%	+0.08%	MPP, AM1.5G, N_2, 40°C	*Science*, 2023, **379**, 690.[43]
1.53	23.8	23.1	23.3	4.7	23.2	-0.08%	-0.08%	MPP, AM1.5G	*Adv. Funct. Mater.*, 2023, **33**, 2300089.[44]
1.53	23.8	23.2	22.6	4.7	22.8	-0.07%	-0.20%	MPP, AM1.5G, air, 30°C	*Nature*, 2023, **620**, 323.[45]
1.55	22.9	20.8	/	4.3	/	-0.26%	/	MPP, AM1.5G, N_2	*Adv. Energy Mater.*, 2023, **13**, 2301066.[46]
1.56	21.1	20.9	/	4.2	/	-0.03%	/	MPP, AM1.5G, air, 30-40%RH, 45°C	*Science*, 2023, **380**, 404.[33]
1.52	23.6	22.8	20.2	4.6	21.9	-0.1%	-0.56%	MPP, AM1.5G, N_2, encapsulated, 50 °C	*Science*, 2023, **382**, 1399.[32]
1.53	22.9	22.8	20.6	4.6	21.8	-0.01%	-0.38%	MPP, w-LED, air, encapsulated, 30-40%RH, 85°C	*Science*, 2024, **386**, 898.[47]
1.53	23.2	22.7	22.0	4.6	22.6	-0.06%	-0.20%	MPP, w-LED, air, encapsulated, 50%RH, 65°C	*Science*, 2024, **384**, 189.[48]
1.55	23.7	23.6	23.0	4.7	23.4	-0.01%	-0.11%	MPP, w-LED, air, encapsulated, 65°C	*Science* 2024, **386**, 187.[49]
1.55	**24.5**	**23.98**	**21.88**	**4.8**	**23.2**	**-0.07%**	**-0.44%**	**MPP, w-LED, N_2, unsealed, 30°C**	**This work**

7. Supplementary References

1. H. Wang, C. Zhu, L. Liu, S. Ma, P. Liu, J. Wu, C. Shi, Q. Du, Y. Hao, S. Xiang, H. Chen, P. Chen, Y. Bai, H. Zhou, Y. Li and Q. Chen, *Adv. Mater.*, 2019, **31**, 1904408.
2. C. Zhu, X. Niu, Y. Fu, N. Li, C. Hu, Y. Chen, X. He, G. Na, P. Liu, H. Zai, Y. Ge, Y. Lu, X. Ke, Y. Bai, S. Yang, P. Chen, Y. Li, M. Sui, L. Zhang, H. Zhou and Q. Chen, *Nat. Commun.*, 2019, **10**, 815.
3. X. Zheng, B. Chen, J. Dai, Y. Fang, Y. Bai, Y. Lin, H. Wei, X. C. Zeng and J. Huang, *Nat. Energy*, 2017, **2**, 17102.
4. H. Meng, K. Mao, F. Cai, K. Zhang, S. Yuan, T. Li, F. Cao, Z. Su, Z. Zhu, X. Feng, W. Peng, J. Xu, Y. Gao, W. Chen, C. Xiao, X. Wu, M. D. McGehee and J. Xu, *Nat. Energy*, 2024, **9**, 536-547.
5. W. Peng, K. Mao, F. Cai, H. Meng, Z. Zhu, T. Li, S. Yuan, Z. Xu, X. Feng, J. Xu, M. D. McGehee and J. Xu, *Science*, 2023, **379**, 683-690.
6. R. H. Bube, *J. Appl. Phys.*, 1962, **33**, 1733.

7. Q. Han, S. H. Bae, P. Sun, Y. T. Hsieh, Y. M. Yang, Y. S. Rim, H. Zhao, Q. Chen, W. Shi, G. Li and Y. Yang, *Adv. Mater.*, 2016, **28**, 2253-2258.
8. V. M. Le Corre, E. A. Duijnstee, O. El Tambouli, J. M. Ball, H. J. Snaith, J. Lim and L. J. A. Koster, *ACS Energy Lett.*, 2021, **6**, 1087-1094.
9. S. Wu, Y. Yan, J. Yin, K. Jiang, F. Li, Z. Zeng, S.-W. Tsang and A. K. Y. Jen, *Nat. Energy*, 2024, **9**, 411-421.
10. W. Tress, N. Marinova, O. Inganas, M. K. Nazeeruddin, S. M. Zakeeruddin and M. Graetzel, *Adv. Energy Mater.*, 2015, **5**, 1400812.
11. D. Bi, W. Tress, M. I. Dar, P. Gao, J. Luo, C. Renevier, K. Schenk, A. Abate, F. Giordano, J.-P. C. Baena, J.-D. Decoppet, S. M. Zakeeruddin, M. K. Nazeeruddin, M. Grätzel and A. Hagfeldt, *Sci. Adv.*, 2016, **2**, e150117.
12. O. Almora, D. Baran, G. C. Bazan, C. Berger, C. I. Cabrera, K. R. Catchpole, S. Erten-Ela, F. Guo, J. Hauch, A. W. Y. Ho-Baillie, T. J. Jacobsson, R. A. J. Janssen, T. Kirchartz, N. Kopidakis, Y. Li, M. A. Loi, R. R. Lunt, X. Mathew, M. D. McGehee, J. Min, D. B. Mitzi, M. K. Nazeeruddin, J. Nelson, A. F. Nogueira, U. W. Paetzold, N.-G. Park, B. P. Rand, U. Rau, H. J. Snaith, E. Unger, L. Vaillant-Roca, H.-L. Yip and C. J. Brabec, *Adv. Energy Mater.*, 2021, **11**, 2002774.
13. O. Almora, C. I. Cabrera, S. Erten-Ela, K. Forberich, K. Fukuda, F. Guo, J. Hauch, A. W. Y. Ho-Baillie, T. J. Jacobsson, R. A. J. Janssen, T. Kirchartz, M. A. Loi, X. Mathew, D. B. Mitzi, M. K. Nazeeruddin, U. W. Paetzold, B. P. Rand, U. Rau, T. Someya, E. Unger, L. Vaillant-Roca and C. J. Brabec, *Adv. Energy Mater.*, 2024, **14**, 2303173.
14. M. Li, H. Li, Q. Zhuang, D. He, B. Liu, C. Chen, B. Zhang, T. Pauporté, Z. Zang and J. Chen, *Angew. Chem., Int. Ed.*, 2022, **61**, e202206914.
15. X. Li, W. Zhang, X. Guo, C. Lu, J. Wei and J. Fang, *Science*, 2022, **375**, 434-437.
16. H. Bi, J. Liu, Z. Zhang, L. Wang, G. Kapil, Y. Wei, A. Kumar Baranwal, S. Razey Sahamir, Y. Sanehira, D. Wang, Y. Yang, T. Kitamura, R. Beresneviciute, S. Grigalevicius, Q. Shen and S. Hayase, *Adv. Sci.*, 2023, **10**, 2304790.
17. R. Chen, J. Wang, Z. Liu, F. Ren, S. Liu, J. Zhou, H. Wang, X. Meng, Z. Zhang, X. Guan, W. Liang, P. A. Troshin, Y. Qi, L. Han and W. Chen, *Nat. Energy*, 2023, **8**, 839-849.
18. H. Li, C. Zhang, C. Gong, D. Zhang, H. Zhang, Q. Zhuang, X. Yu, S. Gong, X. Chen, J. Yang, X. Li, R. Li, J. Li, J. Zhou, H. Yang, Q. Lin, J. Chu, M. Grätzel, J. Chen and Z. Zang, *Nat. Energy*, 2023, **8**, 946-955.
19. M. N. Lintangpradipto, H. Zhu, B. Shao, W. J. Mir, L. Gutiérrez-Arzaluz, B. Turedi, M. Abulikemu, O. F. Mohammed and O. M. Bakr, *ACS Energy Lett.*, 2023, **8**, 4915-4922.
20. T. Pan, W. Zhou, Q. Wei, Z. Peng, H. Wang, X. Jiang, Z. Zang, H. Li, D. Yu, Q. Zhou, M. Pan, W. Zhou and Z. Ning, *Adv. Mater.*, 2023, **35**, 2208522.
21. L. Xie, J. Liu, J. Li, C. Liu, Z. Pu, P. Xu, Y. Wang, Y. Meng, M. Yang and Z. Ge, *Adv. Mater.*, 2023, **35**, 2302752.
22. C. Zhang, H. Li, C. Gong, Q. Zhuang, J. Chen and Z. Zang, *Energy Environ. Sci.*, 2023, **16**, 3825-3836.

23. Q. Zhuang, H. Li, C. Zhang, C. Gong, H. Yang, J. Chen and Z. Zang, *Adv. Mater.*, 2023, **35**, 2303275.
24. J. Liu, J. Chen, P. Xu, L. Xie, S. Yang, Y. Meng, M. Li, C. Xiao, M. Yang and Z. Ge, *Adv. Energy Mater.*, 2024, **14**, 2303092.
25. Z. Zhang, M. Li, R. Li, X. Zhuang, C. Wang, X. Shang, D. He, J. Chen and C. Chen, *Adv. Mater.*, 2024, **36**, 2313860.
26. Y. Zheng, C. Tian, X. Wu, A. Sun, R. Zhuang, C. Tang, Y. Liu, Z. Li, B. Ouyang, J. Du, Z. Li, X. Wu, J. Chen, J. Cai and C.-C. Chen, *Adv. Energy Mater.*, 2024, **14**, 2304486.
27. S. Jiang, R. Wang, M. Li, R. Yu, F. Wang and Z. a. Tan, *Energy Environ. Sci.*, 2024, **17**, 219-226.
28. F. Jiang, W. C. H. Choy, X. Li, D. Zhang and J. Cheng, *Adv. Mater.*, 2015, **27**, 2930-2937.
29. C. Li, Y. Li, Y. Chen, H. Zhang, S.-T. Zhang, Z. Zhang, F. Lin, L. Liang, L. Gong, H. Hao, J. Wang, S. Bao, Y. Yang, M. K. Nazeeruddin, D. Li and P. Gao, *Adv. Funct. Mater.*, 2024, **34**, 2407805.
30. C. Liu, Y. Yang, C. Zhang, S. Wu, L. Wei, F. Guo, G. M. Arumugam, J. Hu, X. Liu, J. Lin, R. E. I. Schropp and Y. Mai, *Adv. Mater.*, 2020, **32**, 1907361.
31. Y. Chen, Y. Shen, W. Tang, Y. Wu, W. Luo, N. Yuan, J. Ding, S. Zhang and W.-H. Zhang, *Adv. Funct. Mater.*, 2022, **32**, 2206703.
32. S. Yu, Z. Xiong, H. Zhou, Q. Zhang, Z. Wang, F. Ma, Z. Qu, Y. Zhao, X. Chu, X. Zhang and J. You, *Science*, 2023, **382**, 1399-1404.
33. S. Zhang, F. Ye, X. Wang, R. Chen, H. Zhang, L. Zhan, X. Jiang, Y. Li, X. Ji, S. Liu, M. Yu, F. Yu, Y. Zhang, R. Wu, Z. Liu, Z. Ning, D. Neher, L. Han, Y. Lin, H. Tian, W. Chen, M. Stolterfoht, L. Zhang, W.-H. Zhu and Y. Wu, *Science*, 2023, **380**, 404-409.
34. S. You, H. Zeng, Y. Liu, B. Han, M. Li, L. Li, X. Zheng, R. Guo, L. Luo, Z. Li, C. Zhang, R. Liu, Y. Zhao, S. Zhang, Q. Peng, T. Wang, Q. Chen, F. T. Eickemeyer, B. Carlsen, S. M. Zakeeruddin, L. Mai, Y. Rong, M. Grätzel and X. Li, *Science*, 2023, **379**, 288-294.
35. L. Tan, J. Zhou, X. Zhao, S. Wang, M. Li, C. Jiang, H. Li, Y. Zhang, Y. Ye, W. Tress, L. Ding, M. Grätzel and C. Yi, *Adv. Mater.*, 2023, **35**, 2205027.
36. H. Hu, D. B. Ritzer, A. Diercks, Y. Li, R. Singh, P. Fassl, Q. Jin, F. Schackmar, U. W. Paetzold and B. A. Nejand, *Joule*, 2023, **7**, 1574-1592.
37. J. Li, J. Dagar, O. Shargaieva, O. Maus, M. Remec, Q. Emery, M. Khenkin, C. Ulbrich, F. Akhundova, J. A. Márquez, T. Unold, M. Fenske, C. Schultz, B. Stegemann, A. Al-Ashouri, S. Albrecht, A. T. Esteves, L. Korte, H. Köbler, A. Abate, D. M. Többens, I. Zizak, E. J. W. List-Kratochvil, R. Schlatmann and E. Unger, *Adv. Energy Mater.*, 2023, **13**, 2203898.
38. Y. Yang, R. Chen, J. Wu, Z. Dai, C. Luo, Z. Fang, S. Wan, L. Chao, Z. Liu and H. Wang, *Angew. Chem., Int. Ed.*, 2024, **63**, e202409689.
39. C. Huang, S. Tan, B. Yu, Y. Li, J. Shi, H. Wu, Y. Luo, D. Li and Q. Meng, *Joule*, 2024, **8**, 2539-2553.
40. S. Li, Y. Xiao, R. Su, W. Xu, D. Luo, P. Huang, L. Dai, P. Chen, P. Caprioglio, K. A. Elmestekawy, M. Dubajic, C. Chosy, J. Hu, I. Habib, A. Dasgupta, D. Guo, Y. Boeije, S. J.

Zelewski, Z. Lu, T. Huang, Q. Li, J. Wang, H. Yan, H.-H. Chen, C. Li, B. A. I. Lewis, D. Wang, J. Wu, L. Zhao, B. Han, J. Wang, L. M. Herz, J. R. Durrant, K. S. Novoselov, Z.-H. Lu, Q. Gong, S. D. Stranks, H. J. Snaith and R. Zhu, *Nature*, 2024, **635**, 874-881.

41. J. Li, C. Jin, R. Jiang, J. Su, T. Tian, C. Yin, J. Meng, Z. Kou, S. Bai, P. Müller-Buschbaum, F. Huang, L. Mai, Y.-B. Cheng and T. Bu, *Nat. Energy*, 2024, DOI: 10.1038/s41560-024-01667-8.
42. L. Zhang, C. Fu, S. Wang, M. Wang, R. Wang, S. Xiang, Z. Wang, J. Liu, H. Ma, Y. Wang, Y. Yan, M. Chen, L. Shi, Q. Dong, J. Bian and Y. Shi, *Adv. Funct. Mater.*, 2023, **33**, 2213961.
43. C. Li, X. Wang, E. Bi, F. Jiang, S. M. Park, Y. Li, L. Chen, Z. Wang, L. Zeng, H. Chen, Y. Liu, C. R. Grice, A. Abudulimu, J. Chung, Y. Xian, T. Zhu, H. Lai, B. Chen, R. J. Ellingson, F. Fu, D. S. Ginger, Z. Song, E. H. Sargent and Y. Yan, *Science*, 2023, **379**, 690-694.
44. H. Bi, Y. Fujiwara, G. Kapil, D. Tavgeniene, Z. Zhang, L. Wang, C. Ding, S. R. Sahamir, A. K. Baranwal, Y. Sanehira, K. Takeshi, G. Shi, T. Bessho, H. Segawa, S. Grigalevicius, Q. Shen and S. Hayase, *Adv. Funct. Mater.*, 2023, **33**, 2300089.
45. P. Shi, Y. Ding, B. Ding, Q. Xing, T. Kodalle, C. M. Sutter-Fella, I. Yavuz, C. Yao, W. Fan, J. Xu, Y. Tian, D. Gu, K. Zhao, S. Tan, X. Zhang, L. Yao, P. J. Dyson, J. L. Slack, D. Yang, J. Xue, M. K. Nazeeruddin, Y. Yang and R. Wang, *Nature*, 2023, **620**, 323-327.
46. L. Zheng, L. Shen, Z. Fang, P. Song, W. Tian, J. Chen, K. Liu, Y. Luo, P. Xu, J. Yang, C. Tian, L. Xie and Z. Wei, *Adv. Energy Mater.*, 2023, **13**, 2301066.
47. Y. Yang, H. Chen, C. Liu, J. Xu, C. Huang, C. D. Malliakas, H. Wan, A. S. R. Bati, Z. Wang, R. P. Reynolds, I. W. Gilley, S. Kitade, T. E. Wiggins, S. Zeiske, S. Suragtkhuu, M. Batmunkh, L. X. Chen, B. Chen, M. G. Kanatzidis and E. H. Sargent, *Science*, 2024, **386**, 898-902.
48. H. Chen, C. Liu, J. Xu, A. Maxwell, W. Zhou, Y. Yang, Q. Zhou, A. S. R. Bati, H. Wan, Z. Wang, L. Zeng, J. Wang, P. Serles, Y. Liu, S. Teale, Y. Liu, M. I. Saidaminov, M. Li, N. Rolston, S. Hoogland, T. Filleter, M. G. Kanatzidis, B. Chen, Z. Ning and E. H. Sargent, *Science*, 2024, **384**, 189-193.
49. D. Gao, B. Li, Q. Liu, C. Zhang, Z. Yu, S. Li, J. Gong, L. Qian, F. Vanin, K. Schutt, M. A. Davis, A. F. Palmstrom, S. P. Harvey, N. J. Long, J. M. Luther, X. C. Zeng and Z. Zhu, *Science*, 2024, **386**, 187-192.